

Masked adversarial neural network for cell type deconvolution in spatial transcriptomics

Lin Huang[†], Xiaofei Liu[†], Shunfang Wang, and Wenwen Min^{*✉}

School of Information Science and Engineering, Yunnan University, Kunming 650091, Yunnan, China

[†]Co-first author. ^{*}Correspondence author: minwenwen@ynu.edu.cn

Abstract—Accurately determining cell type composition in disease-relevant tissues is crucial for identifying disease targets. Most existing spatial transcriptomics (ST) technologies cannot achieve single-cell resolution, making it challenging to accurately determine cell types. To address this issue, various deconvolution methods have been developed. Most of these methods use single-cell RNA sequencing (scRNA-seq) data from the same tissue as a reference to infer cell types in ST data spots. However, they often overlook the differences between scRNA-seq and ST data. To overcome this limitation, we propose a Masked Adversarial Neural Network (MACD). MACD employs adversarial learning to align real ST data with simulated ST data generated from scRNA-seq data. By mapping them into a unified latent space, it can minimize the differences between the two types of data. Additionally, MACD uses masking techniques to effectively learn the features of real ST data and mitigate noise. We evaluated MACD on 32 simulated datasets and 2 real datasets, demonstrating its accuracy in performing cell type deconvolution. All code and public datasets used in this paper are available at <https://github.com/wenwenmin/MACD> and <https://zenodo.org/records/12804822>.

Index Terms—Spatial transcriptomics; Cell-type deconvolution; Masked mechanism; Adversarial learning

I. INTRODUCTION

Spatial transcriptomics (ST) data integrate gene expression profiles with spatial information, providing crucial insights for disease research and targeted therapeutic strategies [1–3]. ST data for cancer research enables the detailed mapping of gene expression patterns within tumors, enhancing our understanding of tumor heterogeneity, microenvironment interactions, and the identification of potential biomarkers [4, 5].

Currently, ST technologies are classified into image-based and sequencing-based methods [6]. Image-based methods, like MERFISH [7] and seqFISH+ [8], offer high spatial resolution but typically detect only a few hundred genes [9, 10]. In contrast, sequencing-based methods, such as 10X Genomics Visium [11], are more widely used because they can detect a broader range of genes. Nevertheless, these methods generally exhibit lower spatial resolution, with each spot potentially containing multiple cells [12].

To address these limitations, cell type deconvolution methods have been developed to disentangle cellular composition within ST data, mitigating the constraints of single-cell resolution. Among existing cell type deconvolution methods, traditional approaches such as CIBERSORT [13] and SPOT-light [14] often directly utilize single-cell RNA sequencing

(scRNA-seq) data as references to infer cellular compositions in ST data. CIBERSORT, initially designed for bulk RNA-seq data, uses linear support vector regression, assuming scRNA-seq profiles represent aggregated ST signals. Similarly, SPOT-light employs non-negative matrix factorization to decompose ST data, assuming scRNA-seq data are suitable references. However, these methods often overlook critical differences: scRNA-seq provides gene expression profiles from individual cells, whereas ST data represent aggregated gene expression from multiple cells [15]. Moreover, variations in sample preparation and technical noise introduce additional discrepancies [16]. These factors may make the deconvolution problem more difficult and the results potentially less accurate. DestVI [17] integrates variational inference with deep learning techniques to estimate cellular composition at each spatial location within tissue samples. Yet, its probabilistic modeling may not fully address the inherent discrepancies between ST and scRNA-seq data. To mitigate these discrepancies, spoint [18] improves alignment by generating simulated ST data and utilizing the maximum mean discrepancy loss function. However, spoint does not specifically target the unique characteristics of real ST data during feature extraction, which may limit its effectiveness.

To this end, we propose MACD, a masked adversarial neural network for cell type deconvolution in spatial transcriptomics. MACD first employs masked mechanism, i.e., a masked autoencoder [19] uncovers the intrinsic characteristics of real ST data. Additionally, MACD employs an adversarial neural network [20] comprising a classifier and a discriminator to optimize the data encoding process. This adversarial setup makes it challenging for the model to distinguish between real and simulated ST data after encoding, thereby minimizing discrepancies and enhancing the consistency and comparability of the data. MACD utilizes labeled simulated ST data to guide model training, enabling accurate inference of cellular composition in simulated ST data. Since the model becomes proficient at distinguishing between real and simulated ST data, it is also expected to perform well in accurately predicting the cellular composition of real ST data.

The main contributions of the paper are as follows:

- A novel adversarial learning-based MACD method is proposed, which aligns real ST data with simulated ST data in the latent space. This approach significantly reduces data discrepancies and enhances consistency, thereby

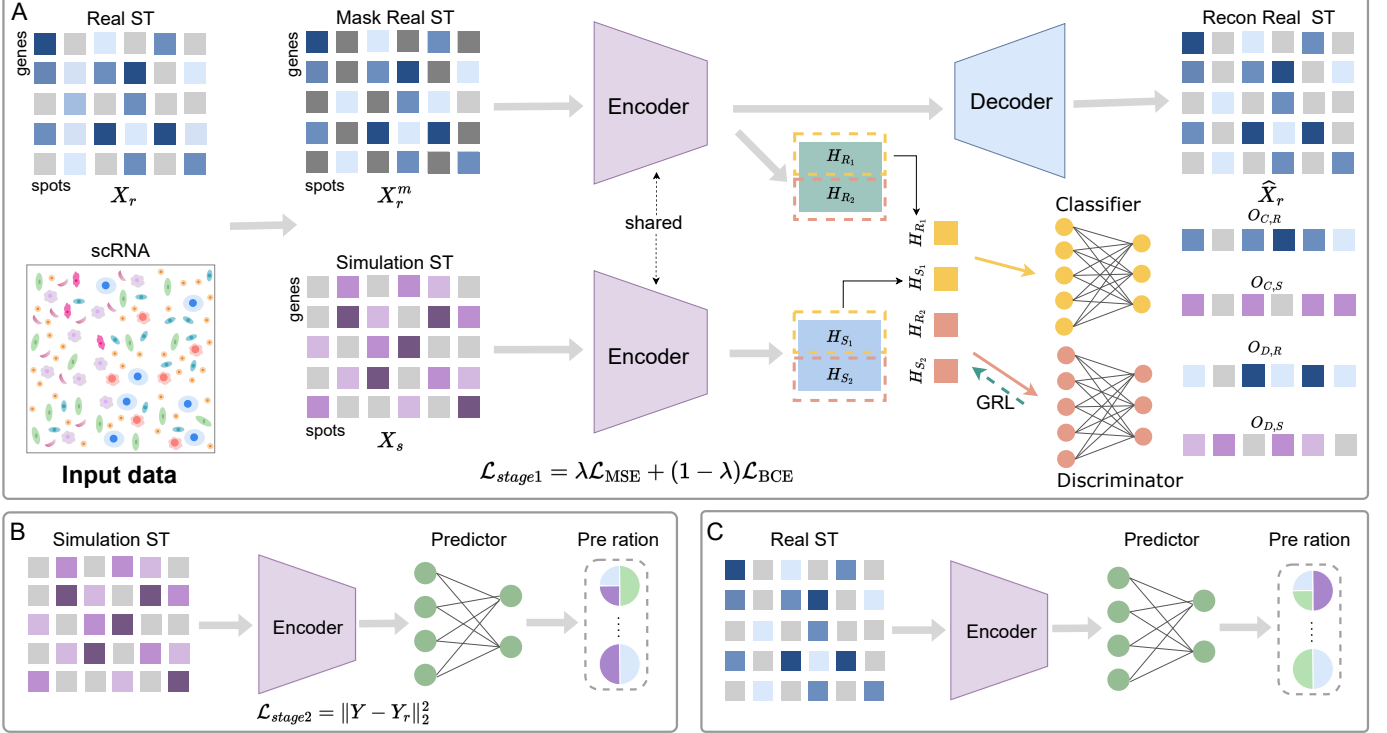


Fig. 1: The network architecture of MACD. The MACD training phase consists of two stages (A) and (B). The simulated and masked ST data are processed by a shared **Encoder** to produce latent variables using masked autoencoder. Adversarial learning is performed on these latent variables, where a classifier distinguishes between real and simulated ST data, and a discriminator, utilizing a Gradient Reversal Layer (GRL), is trained to obscure the differences between them. (C) The trained model is used to infer cell type of the real ST data.

improving the accuracy of cell type deconvolution.

- Integrating a masked autoencoder into MACD uncovers the intrinsic characteristics of real ST data, enhancing the model’s understanding of data nuances.
- Integrating adversarial learning into MACD removes batch effects between real ST and simulated ST data, enabling the supervised learning model built in the latent space of simulated ST data to be effectively applied for cell type deconvolution in real ST data.
- Extensive validation of MACD with 32 simulated datasets and 2 real datasets demonstrates its exceptional robustness and performance across various conditions.

II. PROPOSED METHODS

A. Overview of the proposed MACD method

Herein, a masked adversarial neural network (MACD) is proposed for cell type deconvolution of ST data (Fig. 1). During training, MACD first employs a masked autoencoder to capture the features of the real ST data. Then, adversarial learning aligns real and simulated ST data in the latent space, thereby eliminating discrepancies between them. Finally, supervised learning is conducted on labeled simulated ST data to infer the cell type composition in spatial spots.

B. Masked autoencoder learning

We apply a random masking strategy with a masking rate of ρ to the real ST data matrix (X_r) to obtain the new masked

data matrix (X_r^m) (See Fig. 1A).

The **Encoder** $\mathcal{E}(\cdot)$ processes the masked ST data through two stacked fully connected layers to generate a latent representation of gene expression:

$$H_R = \mathcal{E}(X_r^m; \Theta_e) = W_e^1 \phi(\text{BN}(W_e^0 X_r^m + b_e^0)) + b_e^1 \quad (1)$$

where W_e^0 and W_e^1 are the weight matrices, b_e^0 and b_e^1 are the bias terms, BN denotes batch normalization, and ϕ represents the LeakyReLU activation function.

The **Decoder** $\mathcal{D}(\cdot)$ consists of three fully connected layers used to reconstruct the gene expression from the latent representation:

$$\hat{X}_r = \mathcal{D}(H_R; \Theta_d) \quad (2)$$

Similar to the Encoder, the Decoder employs fully connected layers with their respective weight matrices and bias terms, but it uses three layers instead of two. The detailed structure of the decoder is analogous to the encoder and therefore not expanded here.

$$\mathcal{L}_{\text{MSE}} = \|(\hat{X}_r - X_r) \odot M\|_2^2 \quad (3)$$

where \odot denotes the element-wise multiplication. M_{ij} is 1 or 0. If it is equal, it means that this element is Masked.

C. Adversarial learning

The encoder processes the masked real ST data and the simulated ST data, generating their corresponding latent representations. The first half of each latent representation is fed

TABLE I: Detailed information of each dataset. The scRNA-seq data in Dataset1 to Dataset32 are real data, and the matching ST data are simulated, while the scRNA-seq and ST data in MLN and HDH are both real data.

Datasets	Tissue	source_data				preproce_data					
		Number of Cells/Spots		Number of Genes		Number of Cells/Spots		Number of Genes		Dropout rate	
		SC (Cells)	ST (Spots)	SC	ST	SC (Cells)	ST (Spots)	SC	ST	SC	ST
Dataset1	Human-Brain	10000	1000	33691	46732	10000	1000	4456	4456	81.29%	61.01%
Dataset2	Mouse-Brain	10000	1000	43324	24683	10000	1000	4481	4481	61.05%	76.30%
Dataset3	Human-Liver	3821	1000	18328	19850	3821	1000	1186	1186	90.06%	94.83%
Dataset4	Human-Liver	6948	1000	20007	26160	6948	1000	1171	1171	92.08%	86.78%
Dataset5	Human-Lung	10000	1000	25734	38150	10000	1000	2303	2303	88.12%	95.32%
Dataset6	Human-Lung	10000	1000	25734	26828	10000	1000	1639	1639	84.16%	89.17%
Dataset7	Human-Lung	10000	1000	22066	25199	10000	1000	2831	2831	88.54%	90.01%
Dataset8	Human-Kidney	10000	1000	27345	31489	10000	1000	1531	1531	90.28%	95.15%
Dataset9	Mouse-Kidney	10000	1000	24965	29244	10000	1000	1120	1120	96.76%	95.51%
Dataset10	Human-Heart	10000	1000	17926	29484	10000	1000	1426	1426	82.13%	95.66%
Dataset11	Human-Heart	10000	1000	17926	31580	10000	1000	1426	1426	82.75%	92.18%
Dataset12	Human-Pancreas	2282	1000	21198	17499	2282	1000	1077	1077	79.84%	85.17%
Dataset13	Human-Pancreas	1040	1000	21625	17499	1040	1000	1427	1427	64.85%	85.48%
Dataset14	Human-Pancreas	943	1000	21625	21198	943	1000	1135	1135	66.08%	45.05%
Dataset15	Mouse-Pancreas	1382	1000	19745	14860	1382	1000	1504	1504	67.44%	84.52%
Dataset16	Mouse-Trachea	6937	1000	27084	18388	6937	1000	1034	1034	87.83%	87.74%
Dataset17	Human-Brain	10000	1000	46732	33691	10000	1000	4942	4942	85.99%	79.82%
Dataset18	Mouse-Brain	9999	1000	24683	43324	9999	1000	3227	3227	78.03%	37.39%
Dataset19	Human-Liver	10000	1000	19850	18328	10000	1000	1183	1183	95.88%	87.03%
Dataset20	Human-Liver	8785	1000	26160	20007	8785	1000	1101	1101	90.33%	90.97%
Dataset21	Human-Lung	10000	1000	38150	25734	10000	1000	1813	1813	96.07%	55.29%
Dataset22	Human-Lung	10000	1000	26828	25734	10000	1000	1502	1502	90.63%	44.66%
Dataset23	Human-Lung	10000	1000	25199	22066	10000	1000	2535	2535	92.00%	86.07%
Dataset24	Human-Kidney	10000	1000	31489	27345	10000	1000	1218	1218	95.91%	87.56%
Dataset25	Mouse-Kidney	10000	1000	29244	24965	10000	1000	885	885	96.63%	94.99%
Dataset26	Human-Heart	10000	1000	29484	17926	10000	1000	1077	1077	95.42%	75.15%
Dataset27	Human-Heart	10000	1000	31580	17926	10000	1000	1358	1358	93.58%	77.14%
Dataset28	Human-Pancreas	7944	1000	17499	21198	7944	1000	1148	1148	87.47%	41.59%
Dataset29	Human-Pancreas	8494	1000	17499	21625	8494	1000	1559	1559	87.80%	32.99%
Dataset30	Human-Pancreas	2282	1000	21198	21625	2282	1000	1080	1080	81.47%	38.31%
Dataset31	Mouse-Pancreas	1827	1000	14860	19745	1827	1000	1143	1143	87.02%	24.93%
Dataset32	Mouse-Trachea	7128	1000	18388	27084	7128	1000	1006	1006	88.17%	82.86%
MLN	Murine lymph node	14989	1092	12854	13948	14989	1092	1870	1870	83.41%	61.09%
HDH	Human developing heart	3777	210	15323	38936	3777	209	2373	2373	81.00%	94.01%

into a feedforward neural network (FNN) **Classifier** $\mathcal{F}_C(\cdot)$ to produce predicted labels. The model is optimized to effectively distinguish between real and simulated data:

$$O_{C,R} = \mathcal{F}_C(H_{R_1}; \Theta_C), O_{C,S} = \mathcal{F}_C(H_{S_1}; \Theta_C) \quad (4)$$

where H_{R_1} and H_{S_1} are the first halves of the features from H_R and H_S , respectively. $H_S = \mathcal{E}(X_S; \Theta_e)$, with X_S denoting the simulated ST data. Θ_C represents the classifier's weights and biases. The loss of Classifier:

$$\mathcal{L}_C = f(O_{C,R}, O_{1,T}) + f(O_{C,S}, O_{0,T}) \quad (5)$$

where $O_{i,T} = [i, \dots, i]$ for $i \in \{0, 1\}$, label $i = 1$ indicates real ST data and $i = 0$ indicates simulated ST data. And the binary cross entropy function is defined as

$$f(y_i, \hat{y}_i) = -\frac{1}{N} \sum_{i=1}^N [y_i \log(\hat{y}_i) + (1 - y_i) \log(1 - \hat{y}_i)] \quad (6)$$

Next, the remaining features are fed into a **Discriminator** $\mathcal{F}_D(\cdot)$, implemented as FNN. The discriminator incorporates a gradient reversal layer (GRL), which introduces a gradient reversal during training to prevent it from differentiating between real and simulated data in the latent space:

$$O_{D,R} = \mathcal{F}_D(H_{R_2}; \Theta_D), O_{D,S} = \mathcal{F}_D(H_{S_2}; \Theta_D) \quad (7)$$

where H_{R_2} and H_{S_2} represent the remaining features of H_R and H_S , respectively. Θ_D represents the discriminator's weights and biases. The loss of Discriminator:

$$\mathcal{L}_D = f(O_{D,R}, O_{1,T}) + f(O_{D,S}, O_{0,T}) \quad (8)$$

Thus, the final loss function of the first stage of MACD (Fig. 1A) is as follows:

$$\mathcal{L}_{stage1} = \lambda \mathcal{L}_{MSE} + (1 - \lambda) \mathcal{L}_{BCE} \quad (9)$$

where $\mathcal{L}_{BCE} = \mathcal{L}_C + \mathcal{L}_D$ (See Eq. 5 and Eq. 8) and λ is used to balance the influences of reconstruction loss \mathcal{L}_{MSE} and \mathcal{L}_{BCE} .

D. Supervised prediction learning

The second stage of MACD is a Supervised Prediction Learning module (See Fig. 1B), which shares the **Encoder** with the first stage. The **Predictor** $\mathcal{P}(\cdot)$ consists of two linear layers followed by a softmax layer, specifically designed to infer cell-type proportions from the latent representation:

$$Y = \mathcal{P}(H_S; \Theta_P) = \text{softmax}(W_p^1 \phi(\text{BN}(W_p^0 H_S + b_p^0)) + b_p^1) \quad (10)$$

where W_p^0 and W_p^1 are the weight matrices, b_p^0 and b_p^1 are the bias terms.

The loss function of the second stage of MACD is as follows:

$$\mathcal{L}_{stage2} = \|Y - Y_r\|_2^2 \quad (11)$$

where Y_r represents the ground truth cell-type proportion of simulated ST data.

E. Training process

The training procedure is divided into two phases. Initially, we use Eq. 9 as the training objective. In the subsequent phase, we shift to Eq. 11 as the training objective. These two phases are alternated until the loss functions for both Eq. 9 and Eq. 11 converge.

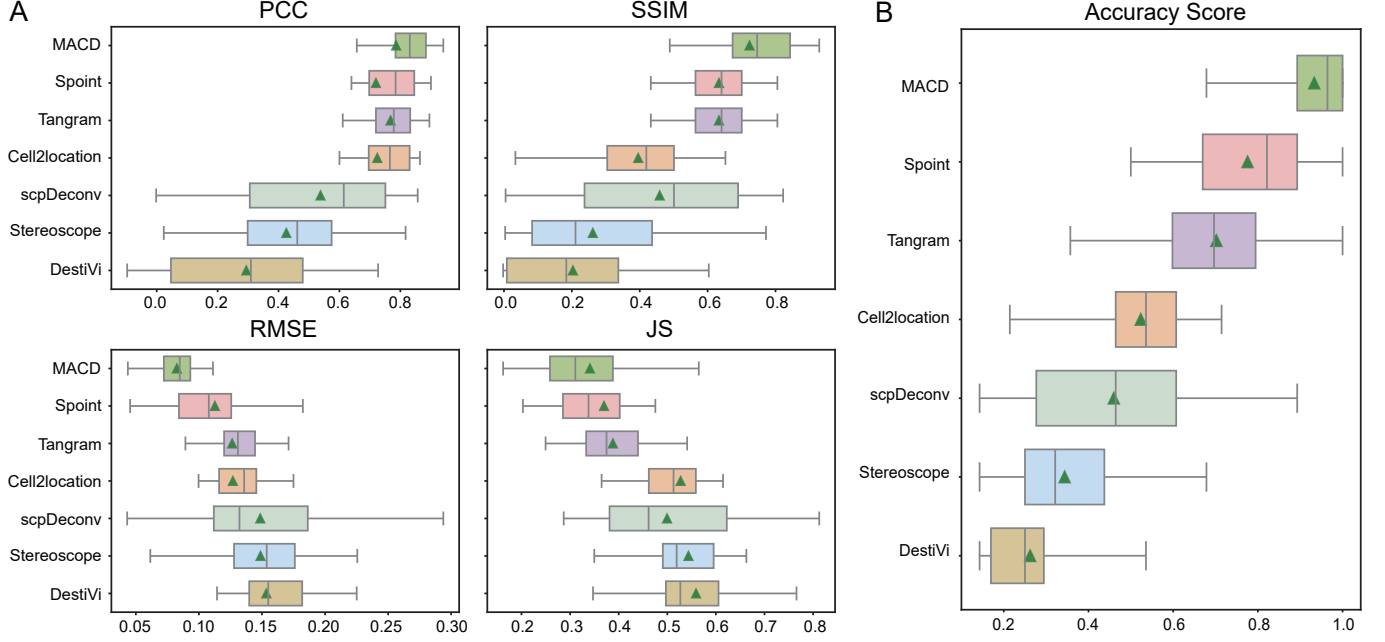


Fig. 2: Performance evaluation of MACD on 32 simulated datasets, with higher PCC, SSIM, and AS values, and lower RMSE and JS values indicating better performance. AS (Accuracy Score) is a composite metric that combines PCC, SSIM, RMSE, and JS. Green triangles represent the mean values, and the middle line represents the median.

F. Predicting process

The trained model applies to the real ST data to predict cell-type proportions:

$$Y_t = \mathcal{P}(\mathcal{E}(X_r; \Theta_e); \Theta_P) \quad (12)$$

where Y_t represents the final predicted cell-type proportions of the real ST data.

G. Evaluation metrics

We use Pearson correlation coefficient (PCC), Jensen-Shannon divergence (JS), root mean square error (RMSE), Accuracy score (AS) and structural similarity index measure (SSIM) to evaluate the proposed method against baselines.

$$\text{PCC} = \frac{\text{cov}(x_i, \hat{x}_i)}{\sigma_i \hat{\sigma}_i} \quad (13)$$

where x_i is the ground truth cell type composition for cell type i , σ_i is its standard deviation, and \hat{x}_i and $\hat{\sigma}_i$ are the predicted values.

$$\text{SSIM} = \frac{(2\hat{u}_i u_i + C_1)(2\text{cov}(x_i, \hat{x}_i) + C_2)}{(\hat{u}_i^2 + u_i^2 + C_1)(\hat{\sigma}_i^2 + \sigma_i^2 + C_2)} \quad (14)$$

where μ_i is the average ground truth cell type composition for cell type i , $\hat{\mu}_i$ is the predicted average, and C_1 and C_2 are constants set to 0.01 and 0.03, respectively.

$$\text{RMSE} = \sqrt{\frac{1}{M} \sum_{j=1}^M (x_{ij} - \hat{x}_{ij})^2} \quad (15)$$

where x_{ij} is the ground truth cell type composition for cell type i in spot j , and \hat{x}_{ij} is the predicted value.

$$\text{JS} = \frac{1}{2} \text{KL} \left(P_i, \frac{\hat{P}_i + P_i}{2} \right) + \frac{1}{2} \text{KL} \left(\hat{P}_i, \frac{\hat{P}_i + P_i}{2} \right) \quad (16)$$

where P_i and \hat{P}_i are the spatial distributions of cell type i in the ground truth and prediction, respectively.

$$\text{AS} = \frac{1}{4} (\text{RANK}_{\text{PCC}} + \text{RANK}_{\text{SSIM}} + \text{RANK}_{\text{RMSE}} + \text{RANK}_{\text{JS}}) \quad (17)$$

where the average PCC/SSIM and RMSE/JS of all deconvolution methods are ranked in ascending and descending order, respectively, to obtain RANK_{PCC} , $\text{RANK}_{\text{SSIM}}$, $\text{RANK}_{\text{RMSE}}$, and RANK_{JS} .

III. EXPERIMENTAL RESULTS

A. Dataset description

This study utilized 32 simulated datasets from the benchmark study [21] and two real datasets from distinct tissues: one from mouse lymph node tissue [17] and the other from human developing heart tissue [22] (Table I). The scRNA-seq data in the 32 simulated datasets were derived from real tissues, with the corresponding ST data being simulated. The ST data (10x Visium) for the mouse lymph node include 1,092 spots, while the scRNA-seq data (10x Chromium) encompass 14,989 cells classified into 15 cell types. For the human developing heart tissue, the ST (ST) data comprise 210 spots, and the scRNA-seq data (10x Chromium) contain 3,777 single cells, identifying 15 distinct cell types.

ST and scRNA-seq data preprocessing. We employed tools such as Seurat [23] and Scanpy [24] to perform cell

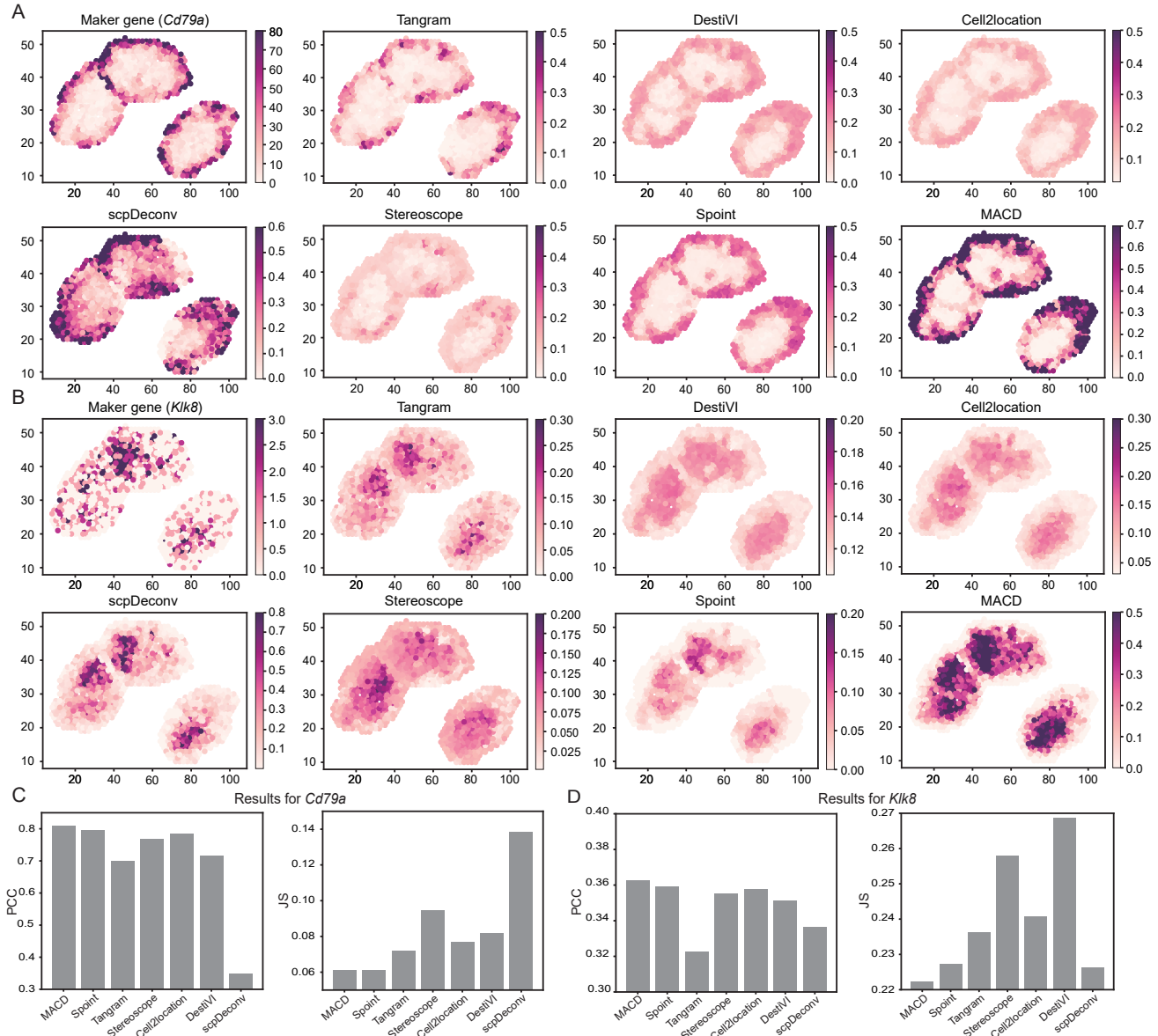


Fig. 3: MACD effectively analyzes both major and rare cell types in the Murine Lymph Node (MLN) dataset. (A) The first panel displays the expression levels of the marker gene *Cd79a*, followed by the proportions of Mature B cells (a rare cell type) estimated by MACD and other methods. (B) The first panel shows the expression levels of the marker gene *Klk8*, followed by the proportions of CD8 T cells (a major cell type) estimated by MACD and other methods. (C) Compares the PCC and JS between MACD and other methods for the marker gene *Cd79a* and the proportion of Mature B cells. (D) Compares the PCC and JS between MACD and other methods for the marker gene *Klk8* and the proportion of CD8 T cells.

clustering on the scRNA-seq data, identify marker genes for each cell type, and retain the top 200 marker genes per cell type. For the ST data, we retained only the genes that intersected between the ST data and the preprocessed scRNA-seq data. Detailed descriptions of each dataset are provided in Table I.

Simulated ST data. The process of generating pseudo-spot based Simulated ST data from scRNA-seq data is referenced in [18]. Simply, based on these single cells from the referenced scRNA-seq data, we generate pseudo-spots through a simulation process to obtain pseudo-spot based **Simulated ST data**.

B. Baseline methods

In this study, we selected six representative state-of-the-art methods:

- Spoint [18]: Spoint utilizes deep learning for feature extraction in spatial transcriptomics data and applies PCA for dimensionality reduction, enhancing cell type deconvolution accuracy.
- Tangram [25]: Tangram employs deep learning to map scRNA-seq data onto ST data, predicting the spatial distribution of cell types.
- Cell2location [26]: Cell2location performs cell-type de-

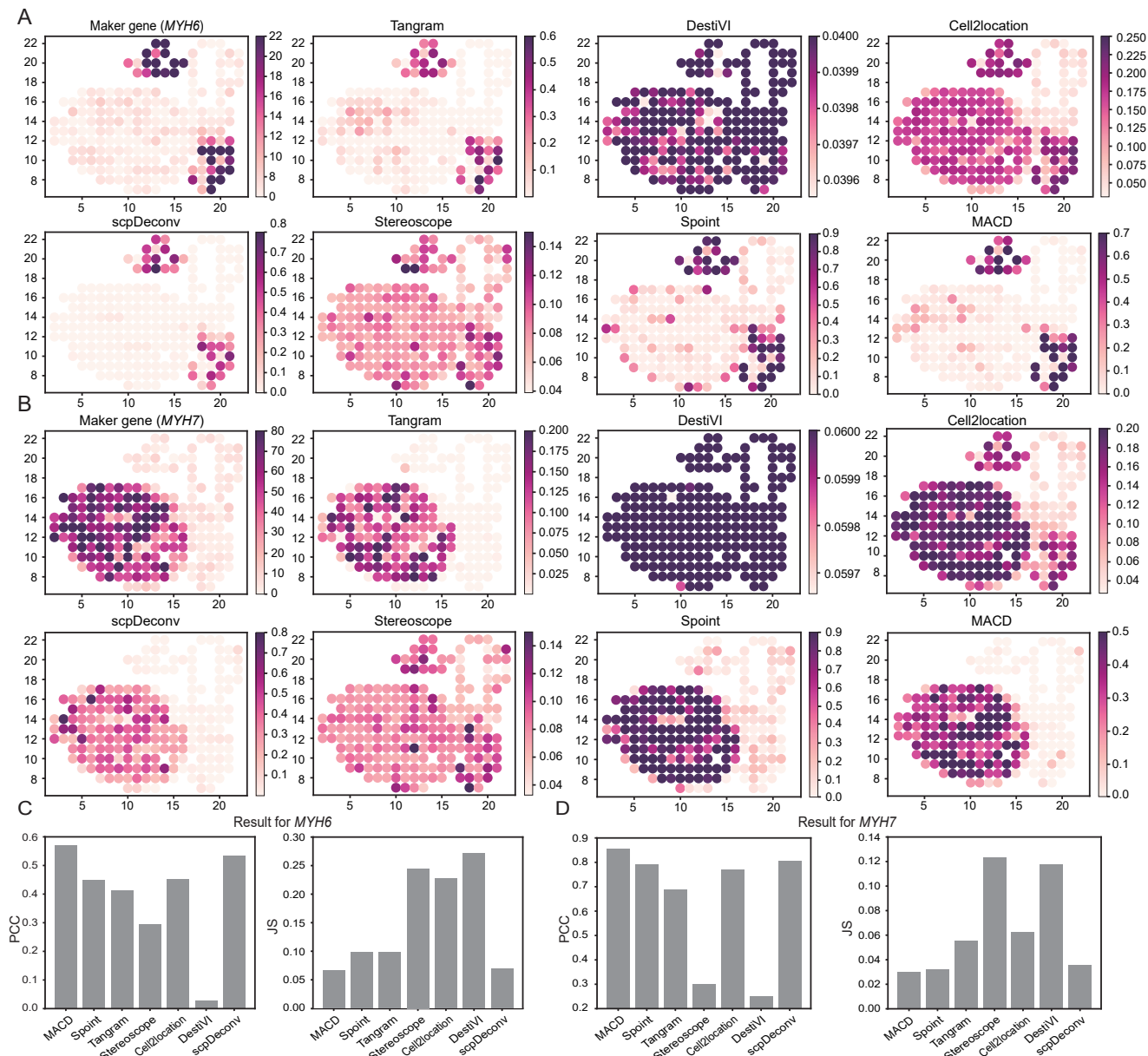


Fig. 4: MACD effectively analyzes both major and rare cell types in the Human Developing Heart (HDH) dataset. (A) The first panel shows the expression levels of the marker gene *MYH6*, followed by the proportions of Atrial cardiomyocytes (a rare cell type) estimated by MACD and other methods. (B) The first panel displays the expression levels of the marker gene *MYH7*, followed by the proportions of Ventricular cardiomyocytes (a major cell type) estimated by MACD and other methods. (C) Compares the PCC and JS between MACD and other methods for the marker gene *MYH6* and the proportion of Atrial cardiomyocytes. (D) Compares the PCC and JS between MACD and other methods for the marker gene *MYH7* and the proportion of Ventricular cardiomyocytes.

convolution of ST data using a hierarchical Bayesian framework to achieve accurate results.

- DestVI [17]: DestVI utilizes variational inference and latent variable models to estimate the proportions of different cell types.
- scpDeconv [27]: scpDeconv combines scRNA-seq data with proteomic data using a domain adversarial auto-encoder to improve the precision of identifying cell types.
- Stereoscope [28]: Stereoscope integrates scRNA-seq and ST data to spatially map cell types by leveraging proba-

bilistic modeling techniques.

C. Implementation Details

All baseline models were implemented with the default parameters specified in their original papers. Experiments were conducted on an NVIDIA RTX 3090 GPU using PyTorch (version 1.12.1) and Python 3.9. The training process was set for 200 epochs, with a batch size of 2048, a learning rate of 0.01 and $\rho = 0.3$.

TABLE II: Ablation experiments on the 32 simulated datasets in terms of the AS metric. AL: Adversarial Learning, mask: Reconstruction loss computed only for the masked points. Full_rec: Full reconstruction loss.

AS(\uparrow)	Dataset1	Dataset2	Dataset3	Dataset4	Dataset5	Dataset6	dataset7	dataset8
MACD (w/o mask, w/o AL)	0.638±0.054	0.563±0.042	0.538±0.082	0.363±0.021	0.425±0.018	0.438±0.052	0.513±0.036	0.413±0.036
MACD (w/ mask,w/o AL)	0.425±0.049	0.813±0.017	0.313±0.051	0.425±0.014	0.475±0.031	0.625±0.008	0.425±0.024	0.413±0.009
MACD (w/o mask, w/ AL)	0.700±0.008	0.363±0.021	0.725±0.018	0.800±0.007	0.525±0.011	0.650±0.035	0.638±0.026	0.800±0.012
MACD (w/ Full_rec, w/o AL)	0.513±0.011	0.375±0.018	0.625±0.034	0.550±0.065	0.575±0.058	0.375±0.016	0.463±0.041	0.475±0.048
MACD	0.725±0.068	0.888±0.007	0.800±0.015	0.863±0.024	0.998±0.001	0.913±0.011	0.963±0.006	0.900±0.015
AS(\uparrow)	Dataset9	Dataset10	Dataset11	Dataset12	Dataset13	Dataset14	Dataset15	Dataset16
MACD (w/o mask, w/o AL)	0.550±0.022	0.425±0.028	0.400±0.008	0.450±0.022	0.400±0.012	0.400±0.062	0.363±0.027	0.513±0.051
MACD (w/ mask, w/o AL)	0.625±0.016	0.375±0.038	0.388±0.012	0.588±0.037	0.763±0.009	0.650±0.007	0.425±0.001	0.400±0.028
MACD (w/o mask, w/ AL)	0.700±0.008	0.825±0.004	0.775±0.011	0.663±0.052	0.638±0.027	0.588±0.006	0.750±0.028	0.563±0.004
MACD (w/ Full_rec, w/o AL)	0.325±0.001	0.425±0.011	0.463±0.037	0.475±0.084	0.325±0.004	0.363±0.012	0.550±0.035	0.588±0.021
MACD	0.800±0.035	0.950±0.005	0.975±0.003	0.825±0.038	0.875±0.008	1.000±0.000	0.913±0.004	0.938±0.006
AS(\uparrow)	Dataset17	Dataset18	Dataset19	Dataset20	Dataset21	Dataset22	Dataset23	Dataset24
MACD (w/o mask, w/o AL)	0.425±0.024	0.750±0.032	0.375±0.018	0.363±0.036	0.588±0.007	0.525±0.041	0.450±0.015	0.425±0.041
MACD (w/ mask,w/o AL)	0.488±0.074	0.400±0.032	0.575±0.091	0.325±0.023	0.650±0.002	0.488±0.024	0.525±0.034	0.888±0.021
MACD (w/o mask, w/ AL)	0.638±0.012	0.438±0.036	0.650±0.055	0.775±0.003	0.650±0.045	0.763±0.026	0.500±0.012	0.338±0.002
MACD (w/ Full_rec,w/o AL)	0.550±0.052	0.488±0.046	0.650±0.062	0.638±0.037	0.238±0.006	0.400±0.073	0.525±0.034	0.563±0.037
MACD	0.900±0.015	0.925±0.003	0.750±0.138	0.900±0.028	0.875±0.014	0.825±0.038	0.998±0.001	0.788±0.022
AS(\uparrow)	Dataset25	Dataset26	Dataset27	Dataset28	Dataset29	Dataset30	Dataset31	Dataset32
MACD (w/o mask, w/o AL)	0.463±0.026	0.413±0.057	0.488±0.002	0.388±0.022	0.613±0.036	0.550±0.047	0.588±0.052	0.538±0.056
MACD (w/ mask,w/o AL)	0.738±0.017	0.300±0.008	0.513±0.022	0.500±0.028	0.800±0.028	0.638±0.029	0.425±0.043	0.313±0.011
MACD (w/o mask, w/ AL)	0.613±0.026	0.763±0.027	0.750±0.052	0.888±0.011	0.488±0.022	0.475±0.008	0.663±0.012	0.525±0.043
MACD (w/ Full_rec,w/o AL)	0.275±0.009	0.613±0.042	0.325±0.004	0.450±0.042	0.400±0.022	0.513±0.012	0.363±0.021	0.738±0.021
MACD	0.913±0.002	0.913±0.011	0.925±0.004	0.775±0.069	0.700±0.105	0.825±0.014	0.963±0.002	0.888±0.037

We evaluated the model performance with different values of λ in Eq. 9. When $\lambda = 0.1$, the average AS for the 32 simulated datasets is 0.61; when $\lambda = 0.5$, it is 0.75; and when $\lambda = 0.9$, it is 0.63. Therefore, $\lambda = 0.5$ was used for all subsequent experiments.

D. Performance of MACD in the 32 simulated datasets

Due to the lack of single-cell resolution in real ST data, it is impossible to precisely quantify the accuracy of our inferred cell type compositions. To assess the performance of MACD in inferring cell type compositions, we used 32 simulated datasets from the benchmark study [21]. These datasets are designed to closely mimic real ST data scenarios, providing high reliability for our evaluation. We compared MACD with six state-of-the-art cell type deconvolution methods in terms of performance.

Our experimental results showed that among the six deconvolution methods, MACD achieved the highest average PCC/SSIM values (0.941/0.929) and the lowest average RMSE/JS values (0.043/0.162) (See Fig. 2A). Furthermore, we evaluated overall performance using the AS. MACD achieved a significantly higher average AS (0.93) compared to other methods (AS = 0.26–0.76) (See Fig. 2B). Overall, these results demonstrate that MACD offers substantial advantages in cell type deconvolution, showing superior performance in both similarity assessment and error measurement. Through comprehensive testing on simulated datasets, MACD has proven its robust capability in predicting complex cell type compositions.

E. Performance of MACD in the MLN dataset

To evaluate the effectiveness of MACD on real tissue samples, we applied it to a mouse lymph node (MLN) dataset [17]. We analyzed mature B cells and CD8 T cells from MLN tissue, where mature B cells produce antibodies and CD8 T cells target infected or abnormal cells. Using the differential analysis

tools provided by Scanpy [24], we identified key marker genes for cell type characterization. Specifically, *Cd79a* was selected as a marker for mature B cells, and *Klk8* was chosen for CD8 T cells. The predicted results of mature B cells and CD8 T cells by MACD closely match the marker gene expression levels (Fig. 3A and Fig. 3B). We performed quantitative evaluation using these marker genes as benchmarks. The PCC between the predicted mature B cells and the marker gene *Cd79a* was 0.8049, with a JS of 0.0612 (Fig. 3C). For CD8 T cells, the PCC with the marker gene *Klk8* was 0.3615, and the JS was 0.2206 (Fig. 3D). Compared to six state-of-the-art deconvolution methods, MACD demonstrated superior performance in predicting cell type proportions, achieving lower error rates.

F. Performance of MACD in the HDH dataset

To further evaluate MACD’s performance on different tissue types, we applied it to the human developing heart (HDH) dataset [22]. We assessed atrial cardiomyocytes using *MYH6* as the marker gene, which are crucial for efficiently transferring blood from the atria to the ventricles and maintaining normal heart function. MACD’s predictions for atrial cardiomyocyte distribution were highly consistent with *MYH6* expression (Fig. 4A), achieving the highest PCC of 0.5721 and the lowest JS of 0.0657 (Fig. 4C). These results highlight MACD’s effectiveness in deconvoluting rare cell types.

Subsequently, we assessed regional-enriched ventricular cardiomyocytes using *MYH7* as the marker gene. Ventricular cardiomyocytes are located in the heart’s ventricles and are critical for systemic blood circulation. The results indicated that MACD’s predicted distribution of ventricular cardiomyocytes closely matched the marker gene (Fig. 4B). In the quantitative assessment (Fig. 4D), MACD achieved the highest PCC of 0.8542 and the lowest JS of 0.0301, confirming its ability

to accurately predict the proportions and spatial distribution of ventricular cardiomyocytes. Overall, these results confirm that MACD effectively performs cell type deconvolution in the HDH dataset.

G. Ablation studies

To evaluate the contributions of the masking and adversarial modules to the MACD model, we conducted a series of ablation experiments (Table II). We specifically aimed to determine if these modules enhance model performance and whether reconstruction loss should be computed on the masked region or the entire ST data. The experiments included a baseline model with only the encoder and predictor, a model with a masking module (reconstruction loss computed only for the masked region), a model with full reconstruction loss, and a model with an adversarial module. The ablation experiments confirm the critical role of the masking and adversarial modules in enhancing the accuracy of cell type proportion predictions.

IV. CONCLUSIONS

To address the challenge of single-cell resolution in spatial transcriptomics (ST) technologies, we present MACD, a masked adversarial neural network designed for precise cell type deconvolution. MACD leverages a masked autoencoder (MAE) to effectively learn latent features from real ST data during encoding and decoding. By employing adversarial learning, MACD aligns real and simulated ST data in a unified latent space, thereby reducing discrepancies. Furthermore, MACD infers cell type compositions through supervised learning on labeled simulated ST data. Evaluations on 32 simulated datasets and 2 real datasets show that MACD significantly outperforms six state-of-the-art deconvolution methods, demonstrating superior performance across these datasets. Ablation studies highlight the critical role of each component in the MACD framework.

ACKNOWLEDGMENT

The work was supported in part by the National Natural Science Foundation of China (62262069, 62062067).

REFERENCES

- [1] S. Jain and M. T. Eadon, "Spatial transcriptomics in health and disease," *Nature Reviews Nephrology*, pp. 1–13, 2024.
- [2] A. Rao, D. Barkley, G. S. França, and I. Yanai, "Exploring tissue architecture using spatial transcriptomics," *Nature*, vol. 596, no. 7871, pp. 211–220, 2021.
- [3] W. Min, Z. Shi, J. Zhang, J. Wan, and C. Wang, "Multimodal contrastive learning for spatial gene expression prediction using histology images," *arXiv:2407.08216*, 2024.
- [4] Q. Wang, Y. Zhi, M. Zi, Y. Mo, Y. Wang, Q. Liao, S. Zhang, Z. Gong, F. Wang, Z. Zeng *et al.*, "Spatially resolved transcriptomics technology facilitates cancer research," *Advanced Science*, vol. 10, no. 30, p. 2302558, 2023.
- [5] W. Min, D. Fang, J. Chen, and S. Zhang, "Dimensionality reduction and denoising of spatial transcriptomics data using dual-channel masked graph autoencoder," *bioRxiv*, 2024. [Online]. Available: <https://doi.org/10.1101/2024.05.30.596562>
- [6] D. Bressan, G. Battistoni, and G. J. Hannon, "The dawn of spatial omics," *Science*, vol. 381, no. 6657, p. eabq4964, 2023.
- [7] K. H. Chen and et al., "RNA imaging: Spatially resolved, highly multiplexed rna profiling in single cells," *Science*, vol. 348, p. aaa6090, 2015.
- [8] C. L. Eng and et al., "Transcriptome-scale super-resolved imaging in tissues by rna seqfish," *Nature*, vol. 568, pp. 235–239, 2019.
- [9] J. R. Moffitt and et al., "Molecular imaging of live tissues and cells using multiplexed error-robust fluorescence in situ hybridization," *Nature Communications*, vol. 9, no. 1, pp. 1–12, 2018.
- [10] X. Li, F. Zhu, and W. Min, "SpaDiT: Diffusion Transformer for Spatial Gene Expression Prediction using scRNA-seq," *arXiv:2407.13182*, 2024.
- [11] X. Genomics, "Spatial transcriptomics: molecular maps of the mammalian brain," *bioRxiv*, 2019.
- [12] J. A. Miller and et al., "Transcriptional landscape of the human brain," *Nature*, vol. 597, no. 7877, pp. 607–614, 2021.
- [13] A. M. a. e. a. Newman, "Robust enumeration of cell subsets from tissue expression profiles," *Nature Methods*, vol. 12, no. 5, pp. 455–457, 2015.
- [14] M. Elosua-Bayes and et al., "Spotlight: seeded nmf regression to deconvolute spatial transcriptomics spots with single-cell transcriptomes," *Nucleic Acids Research*, vol. 49, no. 9, pp. e50–e50, 2021.
- [15] T. Stuart, A. Butler, and et al., "Comprehensive integration of single-cell data," *Cell*, vol. 177, no. 7, pp. 1888–1902, 2019.
- [16] S. Rybakov, V. Ponomarev, and et al., "Technical considerations for single-cell transcriptomics," *Nature Communications*, vol. 11, no. 1, p. 1234, 2020.
- [17] R. e. a. Lopez, "Destvi identifies continuums of cell types in spatial transcriptomics data," *Nature Biotechnology*, vol. 40, pp. 1360–1369, 2022.
- [18] H. Xu and et al., "Spacel: deep learning-based characterization of spatial transcriptome architectures," *Nature Communications*, vol. 14, p. 7603, 2023.
- [19] K. He, X. Chen *et al.*, "Masked autoencoders are scalable vision learners," in *CVPR*, 2022, pp. 16 000–16 009.
- [20] F. Wang, F. Yang, L. Huang, W. Li, J. Song, R. B. Gasser, R. Aebbersold, G. Wang, and J. Yao, "Deep domain adversarial neural network for the deconvolution of cell type mixtures in tissue proteome profiling," *Nature Machine Intelligence*, vol. 5, no. 11, pp. 1236–1249, 2023.
- [21] B. Li, W. Zhang, and et al., "Benchmarking spatial and single-cell transcriptomics integration methods for transcript distribution prediction and cell type deconvolution," *Nature Methods*, vol. 19, p. 662–670, 2022.
- [22] M. Asp, S. Giacomello, and et al., "A spatiotemporal organ-wide gene expression and cell atlas of the developing human heart," *Cell*, vol. 179, no. 7, p. 1647–1660.e19, 2019.
- [23] Y. Hao and et al., "Integrated analysis of multimodal single-cell data," *Cell*, vol. 184, pp. 3573–3587.e29, 2021.
- [24] F. A. Wolf and et al., "Scanpy: large-scale single-cell gene expression data analysis," *Genome Biology*, vol. 19, p. 15, 2018.
- [25] T. Biancalani and et al., "Deep learning and alignment of spatially resolved single-cell transcriptomes with tangram," *Nature Methods*, vol. 18, p. 1352–1362, 2021.
- [26] V. Kleshchevnikov and et al., "Cell2location maps fine-grained cell types in spatial transcriptomics," *Nature Biotechnology*, vol. 40, p. 661–671, 2022.
- [27] F. Wang and et al., "Deep domain adversarial neural network for the deconvolution of cell type mixtures in tissue proteome profiling," *Nature Machine Intelligence*, vol. 5, pp. 1236–1249, 2023.
- [28] A. Andersson, J. Bergenstråhle, M. Asp, and et al., "Spatial mapping of cell types by integration of transcriptomics data," *Nature Biotechnology*, vol. 38, pp. 635–640, 2020.